Evaluation of the SPOT/VEGETATION Collection 3 reprocessed dataset: Surface reflectances and NDVI

Carolien Toté[a,*], Else Swinnen[a], Sindy Sterckx[a], Dennis Clarijs[a], Carine Quang[b], Ronny Maes[a]

[a] Flemish Institute for Technological Research (VITO), Remote Sensing Unit, Boeretang 200, B-2400 Mol, Belgium
[b] Communication & Systèmes (CS), Av. Galilée 22, 92350 Le Plessis Robinson, France

A B S T R A C T

After the end of the 'Satellite Pour l'Observation de la Terre' (SPOT) VEGETATION (SPOT/VGT) mission in May/2014, the SPOT/VGT data archive, consisting of raw data coming from both the VEGETATION 1 (VGT1) and VEGETATION 2 (VGT2) instruments, was reprocessed, aiming at improved cloud screening and correcting for known artefacts such as the smile pattern in the VGT2 Blue band and the Sun-Earth distance bug in Top-of-Atmosphere reflectance calculation, with the objective of improving temporal consistency. The aim of this paper is to inform the user community of the changes in and the evaluation of the new SPOT/VGT Collection 3 (VGT-C3). The evaluation of the reprocessing is based on (i) the relative comparison between SPOT/VGT Collection 2 (VGT-C2) and VGT-C3 surface reflectances and Normalized Difference Vegetation Index (NDVI), (ii) consistency analysis between VGT1-C3 and VGT2-C3, and (iii) the comparison of the archive with external datasets from METOP/Advanced Very High Resolution Radiometer (AVHRR) and TERRA/Moderate Resolution Imaging Spectroradiometer (MODIS). Surface reflectances are slightly higher after the reprocessing, with larger differences in July compared to January, caused by the corrected Sun-Earth distance modelling. For NDVI, the overall impact of the reprocessing is relatively small and differences show no seasonality. Trends in the differences over the years are related to changes in calibration coefficients. Systematic differences between VGT1-C3 and VGT2-C3 surface reflectance are well below 1%, with largest bias between VGT1 and VGT2 for the NIR band and the NDVI (VGT2 > VGT1, especially for larger NDVI values). Both the comparison with METOP/AVHRR (surface reflectance and NDVI) and TERRA/MODIS (NDVI) reveal trends over time: systematic bias between VGT2 and METOP/AVHRR tends to decrease over time, while comparison with TERRA/MODIS indicates an increasing bias between VGT2 and MODIS. VGT2 NDVI seems to be gradually evolving to slightly larger values, which is consistent with the change in overpass time of VGT2 and the different illumination conditions caused by the orbital drift of the sensor. Results demonstrate however the SPOT/VGT-C3 archive is more stable over time compared to the previous archive, although bidirectional reflectance distribution function (BRDF) normalization is recommended in order to correct for bidirectional effects.

1. Introduction

The VEGETATION programme, involving partners in France, Belgium, Sweden, Italy, and the European Commission, controlled and maintained the 'Satellite Pour l'Observation de la Terre' (SPOT) VEGETATION (VGT) sensors and distributed the imagery and products derived from them. For over 15 years, the Flemish Institute for Technological Research (VITO) hosted the prime user segment of both VEGETATION 1 (VGT1) and VEGETATION 2 (VGT2) multispectral instruments on board SPOT4, launched in March/1998 and SPOT5, launched in May/2002 (Deronde et al., 2014). The switch from VGT1 to VGT2 was made in February/2003, because the onboard star tracker of

SPOT5 allowed for higher geometric performances for VGT2 in comparison to VGT1. The role of the SPOT/VGT processing facility at VITO (also called CTIV, 'Centre de Traitement d'Images VEGETATION') was to ingest, process and archive all SPOT/VGT data, and to distribute standard derived products to the user community (Passot, 2001).

SPOT/VGT data are widely used to monitor environmental change and the evolution of vegetation cover in different thematic domains such as: long-term, large-scale vegetation status monitoring and climate change studies (e.g. Atzberger and Eilers, 2011; Delbart et al., 2006; Fensholt et al., 2009; Lhermitte et al., 2011; Lupo et al., 2001; Tonini et al., 2012), agricultural monitoring and yield estimations (e.g. Durgun et al., 2016; Rembold et al., 2013; Vrieling et al., 2014), land cover/

land use characterization (e.g. Bartholomé and Belward, 2005; Boles et al., 2004; Carreiras et al., 2006; Immerzeel et al., 2005; Kamthonkiat et al., 2005), monitoring of forest fires and burned areas (e.g. Fraser and Li, 2002; Lasaponara, 2006; Tansey et al., 2008; Zhang, 2003), and many other applications.

In the past years, several partial reprocessing campaigns have been implemented in order to improve calibration of both VGT1 and VGT2 (Bartholomé et al., 2006), resulting in VGT Collection 2 (VGT-C2), which was released in 2006 (for VGT2-C2) and 2010 (for VGT1-C2). After the end of the SPOT/VGT mission in May/2014, the complete data archive was reprocessed. The aim of the reprocessing was to apply an improved cloud screening algorithm and to correct for known artefacts such as the known smile pattern in the VGT2 Blue band (i.e. View Zenith Angle dependency of the Top-Of-Atmosphere (TOA) reflectance values) as observed by various authors (Bouvet, 2014; Sterckx et al., 2013) and the error in Sun-Earth distance modelling in TOA reflectance calculation, thereby improving consistency over time. All instrument calibration parameter updates and improved processing algorithms were provided by the VEGETATION Image Quality Centre (QIV) located at 'Centre National d'Études Spatiales' (CNES). The reprocessing of the complete VGT collection has led also, to some extent, to an improved consistency with the Project for On-Board Autonomy–Vegetation (PROBA-V) satellite (Swinnen and Toté, 2017). PROBA-V was launched in May/2013 and was designed to bridge the gap in space-borne vegetation measurements between the SPOT/VGT mission (March/1998–May/2014) and the Sentinel-3 satellites (from February/2016 onwards) (Dierckx et al., 2014; Sterckx et al., 2014).

This paper discusses the changes in and the evaluation of the new SPOT/VGT Collection 3 (VGT-C3). VGT-C3 products are distributed through the Product Distribution Facility (PDF) (http://www.vito-eodata.be/), supporting the consultation, viewing, download, ordering, subscription, and delivery of the SPOT/VGT, PROBA-V and Copernicus Global Land Service products. The Mission Exploitation Platform (MEP) (http://proba-v.vgt.vito.be/content/mep) provides tools to visualize and analyse large time series of PROBA-V and SPOT/VGT data (Goor et al., 2016).

This manuscript is organized as follows. First we describe the modifications in the SPOT/VGT processing chain and the materials and methods used. Then we evaluate VGT-C3 focusing on three aspects. In first instance, the entire new archive (VGT-C3) is compared against the previous version (VGT-C2), in order to quantify the effect of the changes applied in the reprocessing. Next, the consistency between data obtained from the VGT1 and VGT2 instruments within VGT-C3 (i.e. VGT1-C3 and VGT2-C3) is evaluated: although data derived from VGT1 and VGT2 are normally used as one single dataset, these datasets originate from two sensors with very similar but not identical characteristics. Finally, in order to evaluate the temporal consistency of the entire reprocessed archive, it is compared against two reference time series, i.e. TERRA/Moderate Resolution Imaging Spectroradiometer (MODIS) (Normalized Difference Vegetation Index, NDVI) and METOP/Advanced Very High Resolution Radiometer (AVHRR) (surface reflectance and NDVI).

2. Modifications in the SPOT/VEGETATION processing chain

2.1. Absolute and multi-angular calibration

This section describes the main updates to the instrument calibration parameters as provided by QIV. In VGT-C3, the absolute calibration parameters and multi-angular calibration (or equalization) coefficients were revised.

2.1.1. General description of SPOT/VEGETATION calibration processes

The optical imaging instrument design uses four independent cameras, one for each spectral band, with each one covering the whole Field Of View (FOV) thanks to a linear array of 1728 detectors (or pixels). In the calculation of the TOA radiance L_{TOA} from the observed digital number (DN), both the absolute and equalization coefficients need to be taken into account simultaneously:

$$L_{TOA,i,k} \sim \frac{DN_{i,k}}{A_k . g_{i,k}} \tag{1}$$

where the subscripts i and k identify respectively the across track pixel (or detector) and the spectral band, DN is the raw digital output, A is the absolute calibration coefficient, g is the equalization coefficient. All these parameters vary over time.

For each spectral band, absolute calibration is thus the estimation of A_k, a global parameter independent of the considered pixel, whereas multi-angular calibration refers to variation of the instrument response with viewing angle or pixel, i.e., estimation of the equalization coefficients $g_{i,k}$.

Multi-angular calibration was performed for both VGT instruments before launch and regularly assessed in flight to monitor variations over the FOV, due mainly to heavy irradiations and aging of the different parts of the sensor (Fougnie et al., 2000). To allow these in-flight verifications, the coefficients $g_{i,k}$ were split into three terms according to the following equation:

$$g_{i,k} = P_{i,k} . GLF_{i,k} . GHF_{i,k} \tag{2}$$

GHF is a high-frequency term which refers to variation of the sensitivity of the elementary detector. P is a polynomial fit refering to variation of the optic transmission which slightly decreases when the viewing angle increases. GLF is a low-frequency term which refers mainly to smooth variations of the optic transmission that cannot be modeled by the polynomial function P.

To assess the in-flight absolute calibration parameters and the equalization coefficients, different vicarious calibration methods are applied, using the following natural targets: Rayleigh scattering, sun glint, deep convective clouds and desert sites (Henry and Meygret, 2001). The Rayleigh calibration is based on the idea that the apparent TOA radiance in Blue and Red observed over a clear ocean mainly results from atmospheric molecular scattering. This Rayleigh scattering is very well modeled and used for absolute and multi-angular calibrations. The calibration over sun glint allows to inter-calibrate the Blue, NIR and SWIR bands with respect to the Red band. It is similar to the Rayleigh scattering method, except that the geometrical viewing is set to observe the sun's reflection over the sea: because of the viewing constraints, this method cannot be used for multi-angular calibration. The calibration over clouds assumes that over thick clouds and under certain conditions of acquisition, cloud reflectance is the main contributor to the observed signal. The spectrally-independent properties of deep convective clouds in the visible and NIR bands allow calibration of the Blue and NIR bands with respect to the Red band. Finally, the principle of cross-calibration of sensors over desert sites is used to model the reflectance that the reference sensor (REF) would have measured in the same geometrical conditions and the same spectral bands as the sensor to calibrate (CAL). The signal acquired by CAL is then calibrated using the modeled radiance deduced from REF. Since desert sites are very stable targets in time, this method is also used for multi-temporal calibration, in particular to assess the temporal evolution of A_k (Lachérade et al., 2013).

Finally, all these vicarious calibration methods allow validation of the behavior and the stability of the on-board calibration lamp used to monitor the cameras sensitivity for the four spectral bands (Blue, Red, NIR and SWIR).

2.1.2. Multi-angular calibration

The combination of the on-board lamp, the calibration over clouds and the calibration over Rayleigh scattering allows characterization of the in-flight instrument angular response (i.e. the equalization coefficients) in the Blue, Red and NIR bands. In the SWIR band, only the on-
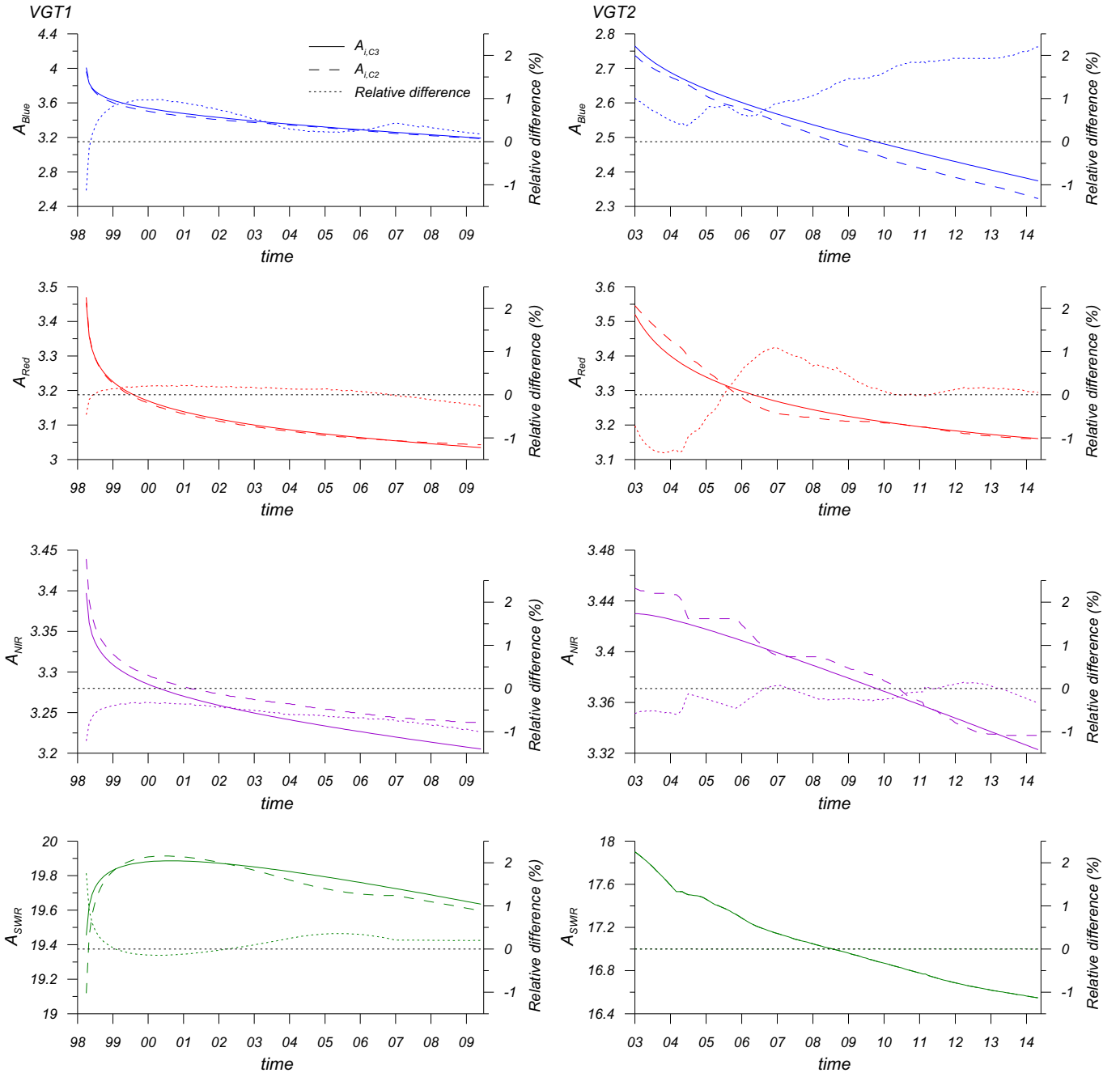
Fig. 1. Evolution of the absolute calibration coefficients of VGT1 (left, 1998–2009) and VGT2 (right, 2003–2014) per band (i): Collection 2 ($A_{i,C2}$, dashed line, left axes) and Collection 3 ($A_{i,C3}$, solid line, left axes) and relative difference ($A_{i,C3} - A_{i,C2}$) / $A_{i,C2}$ · 100% (dotted line, right axes), time on the X-axis in years (YY). The black dotted line indicates a relative difference equal to zero. Note that for the SWIR band no update to the absolute calibration coefficients was applied.

board calibration system can deliver information on the evolution of the VGT angular response. In VGT-C2, the equalization coefficients $g_{i,k}$ were kept constant to their pre-launch values. Verifications of the in-flight multi-angular calibration however showed an evolution of the in-flight $GLF_{i,k}$ coefficients compared to their corresponding pre-launch coefficients.

For VGT-C3, these time-dependent variations were taken into account before proceeding to the absolute calibration. Since characterization of the multi-angular calibration in the SWIR band by the on-board lamp could not be validated by a vicarious calibration method, the equalization coefficients of the SWIR band were not updated. Therefore in VGT-C3, only the multi-angular calibration in the Blue, Red and NIR bands were revised. The methodology applied to carry out

these calibration processes is described below.

In the Blue, Red and NIR bands, the correction of the equalization is done through the reevaluation of the $GLF_{i,k}$. C3 coefficients were generated thanks to a low-frequency correction term GLF^{corr} applied to the pre-launch coefficients $g_{i,k}$, as follows:

$$g_{i,k}^{C3} = \frac{GLF_{i,k}^{corr}}{\langle GLF_{i,k}^{corr} \cdot g_{i,k} \rangle_i} \cdot g_{i,k} \tag{3}$$

where the operator $\langle X \rangle_i$ is the mean of X over the pixels i, and GLF^{corr} is the time-dependent equalization of the instrument angular response. GLF^{corr} profiles (one per spectral band k) were estimated based on the analysis of the calibration over clouds, over Rayleigh scattering, and
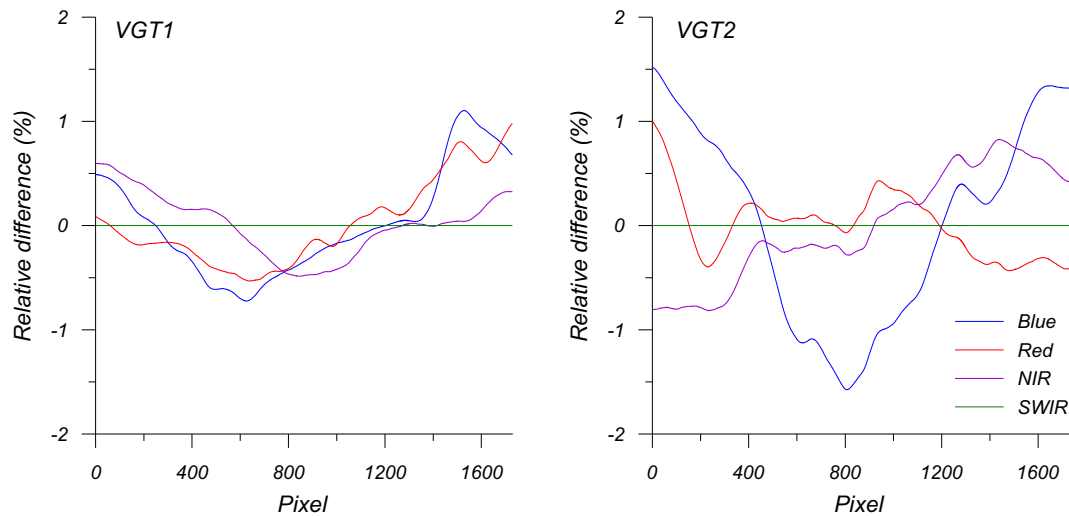
Fig. 2. Relative difference $(g_{i,C3} - g_{i,C2}) / g_{i,C2} \cdot 100\%$ of VGT1 on 12/01/2001 (left) and VGT2 on 30/09/2009 (right), with g the equalization coefficient per pixel i.
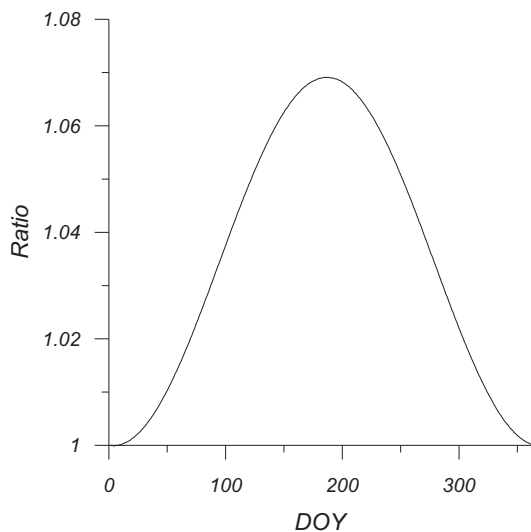

Fig. 3. Ratio between TOA reflectance values in VGT-C3 and VGT-C2 related to correction of Sun-Earth distance modelling. Evolution according to day of year (DOY).

from the on-board lamp. To carry out this analysis, > 200,000 measurements were selected for VGT1, and 400,000 for VGT2, covering their whole lifetime.

For VGT2, calibration results over Rayleigh scattering, completed when available by calibration results over clouds, showed a temporal evolution of the instrument angular response up to 2010, then a stabilised period between 2010 and 1013. In order to estimate the temporal evolution of the correction term GLF^{corr}, the monthly on-board lamp profile was used, following the relation:

$$GLF_{i,k}^{corr}(t) = GLF_{i,k}^{corr}(t_{ref}) \times \frac{GLF_{i,k}^{Lamp}(t)}{GLF_{i,k}^{Lamp}(t_{ref})} \qquad (4)$$

where t is the date from the first day after launch to the end of life of VGT2.

For VGT1, the same method was applied for the Blue band. However, for the Red and NIR bands, the lack of calibration data over clouds and the very high dispersion of Rayleigh scattering measurements made the term $GLF_{i,k}^{corr}(t_{ref})$ impossible to model. By default, the term was considered flat over the FOV, with t_{ref} corresponding to the start of VGT1 (March/1998), thus assuming that the multi-angular calibration was perfect in the early days of VGT1.

2.1.3. Absolute calibration

Once the new equalization coefficients $g_{i,k}^{C3}$ were generated, absolute calibration parameters could be updated for the whole lifetime of VGT1 and VGT2, aiming to improve the stability of the instrument responses over their lifetime.

For each of the four VGT2 bands, the temporal drift of the absolute calibration parameter A_k was estimated using cross-calibration with the MODIS instruments over desert sites. MODIS is considered to be a good reference for VGT2 for three main reasons: (i) both MODIS instruments were launched in 2002, allowing consistent monitoring of VGT2 over large part of its lifetime, (ii) VGT2 and MODIS have similar viewing conditions for solar zenith angles below 35° (Lachérade et al., 2013), and (iii) the good spectral matching of VGT2 and MODIS bands.

Temporal drift was first analysed using time series of desert cross-calibration results of VGT2 with respect to MODIS. Second, a polynomial fit was applied to these time series in order to model the relative temporal drift of A_k. Finally, the absolute level of each fit (one per spectral band) was adjusted on a weighted mean of all relevant calibration measurements (Rayleigh scattering, over-clouds and Sun glint methods) during a selected stable period (2010–2013). However, for the SWIR band, the polynomial fit was less adjusted to the vicarious calibration measurements than the C2 absolute calibration parameters for the first year of the instrument. Besides, the new absolute calibration parameters did not result in significant drift correction, compared to the C2 absolute calibration. For these two reasons, the C2 absolute calibration was not updated for the VGT2 SWIR band.

For VGT1, only cross-calibration results over desert sites were used for the absolute calibration, since too few calibration results over clouds were available, results of Rayleigh scattering calibration were too dispersed and no calibration over sun glint was available for VGT1. As a consequence, the absolute level for each of the four bands of VGT1 was adjusted with cross-calibration results over desert sites of VGT1 with respect to recalibrated VGT2 (i.e. after the application of VGT2-C3 calibration coefficients).

2.1.4. Comparison between C2 and C3 absolute calibration

For VGT1 (Fig. 1, left), over all bands, the differences in absolute calibration coefficients between C2 and C3 are relatively small (< 1%), with in general the largest differences in the first year (1998 until mid 1999). Largest differences are observed for A_{NIR}, with relative differences up to -1%, resulting in increased $L_{TOA,NIR}$.

The changes in absolute calibration for VGT2 are larger (Fig. 1, right). The difference between $A_{Blue,C2}$ and $A_{Blue,C3}$ gradually increases to up to 2.2%, resulting in a gradual reduction of $L_{TOA,Blue}$. For Red, the
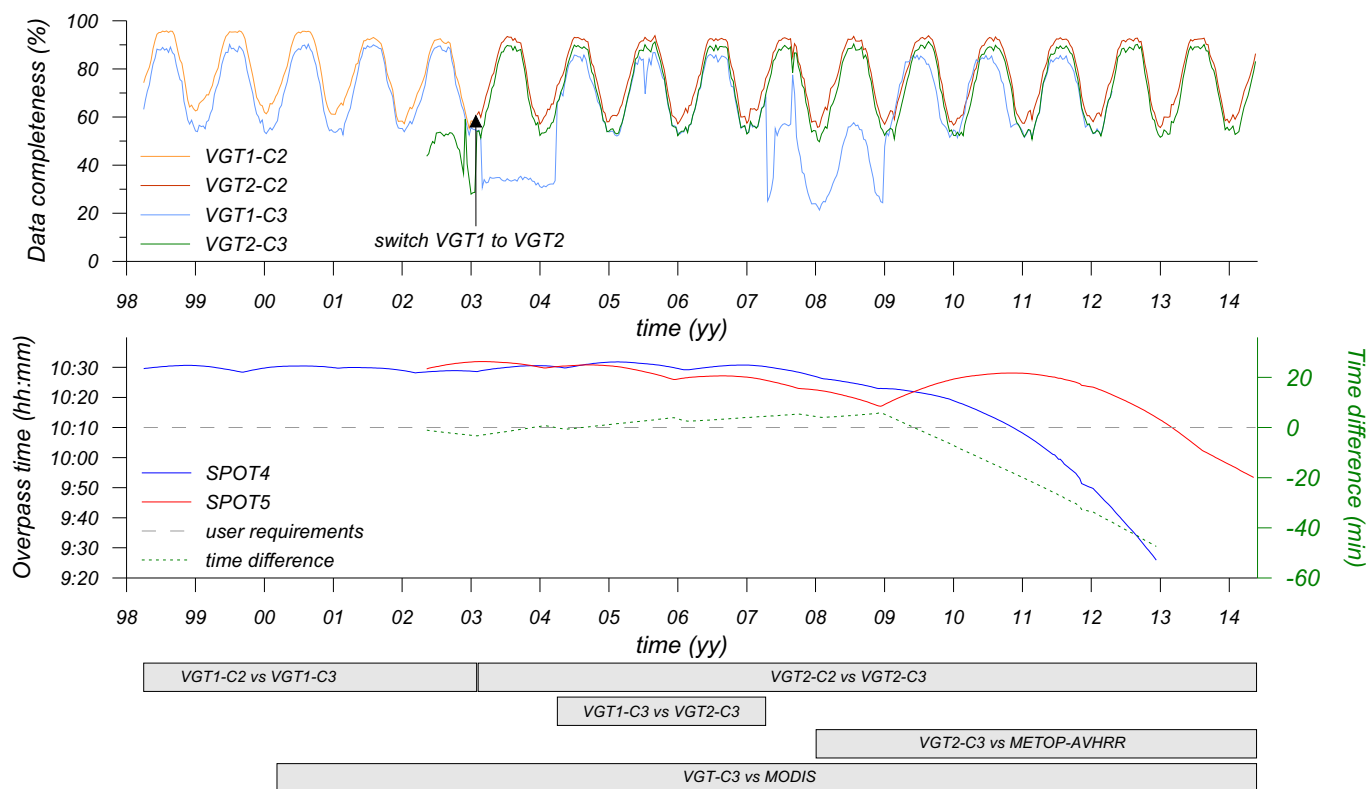
Fig. 4. Top: Data completeness (%) of 10-daily maximum value NDVI composites over land; Middle: Equator local overpass time of SPOT4 (blue) and SPOT5 (red) and the user requirements limit (grey) (left axis), and overpass time difference SPOT4-SPOT5 (green, right axis); Bottom: time periods used in the evaluation. (For interpretation of the references to color in this figure legend, the reader is referred to the web version of this article.)

Table 1

Sampling schemes used to evaluate the comparison between different data sets. The X marks when a constraint is used in a specific sampling scheme.

Constraint	'All constraints'	'Limited'	'Status Map'
Clear observations	X	X	X
Identical day of observation	X		
VZA < 30°	X	X	
No mixed scatter observations	X	X	
Sampling scheme is used in the comparison of	VGT-C2 vs. VGT-C3	VGT1 vs. VGT2	VGT vs. external data

Table 2

Validation metrics calculated between VGT1-C2 and VGT1-C3 (April/1998–January/2003), using the '*All constraints*' sampling scheme.

	a	b	R^2	RMSD	RMPDs	RMPDu	MBE
All dekads (N = 174)							
Blue	− 0.01	0.9800	0.9479	0.91	0.13	0.90	0.11
Red	− 0.07	0.9933	0.9954	0.62	0.15	0.60	0.14
NIR	− 0.27	1.0229	0.9827	1.25	0.35	1.20	− 0.29
SWIR	0.25	1.0202	0.9924	1.13	0.70	0.88	− 0.67
NDVI	0.0058	1.0001	0.9956	0.0231	0.0059	0.0223	− 0.0059
1st dekads of January (N = 5)							
Blue	− 0.31	0.9373	0.9535	1.15	0.75	0.87	0.70
Red	− 0.21	0.9603	0.9978	0.94	0.81	0.47	0.70
NIR	− 0.40	0.9782	0.9923	1.30	0.98	0.85	0.96
SWIR	− 0.05	0.9915	0.9988	0.62	0.26	0.57	0.24
NDVI	0.0075	0.9991	0.9960	0.0233	0.0072	0.0222	− 0.0072
1st dekads of July (N = 5)							
Blue	0.11	1.0349	0.9509	0.87	0.28	0.83	− 0.24
Red	− 0.05	1.0278	0.9971	0.53	0.29	0.44	− 0.18
NIR	− 0.42	1.0639	0.9871	1.58	1.27	0.95	− 1.16
SWIR	0.13	1.0578	0.9939	1.52	1.34	0.71	− 1.24
NDVI	0.0058	0.9967	0.9891	0.0241	0.0041	0.0238	− 0.0040

difference varies over the years: from the start of operations until June/2005, $A_{Red,C3} < A_{Red,C2}$, resulting in up to 1.3% higher $L_{TOA,Red}$, while from August/2005 onwards, $A_{Red,C3} > A_{Red,C2}$, resulting in up to 1.1% lower $L_{TOA,Red}$. Since 2009 only marginal differences are observed. For NIR, the difference varies over the years, but overall the magnitude of the difference is limited.

The change in the equalization over the field of view varies only slightly over time. The relative differences respectively for VGT1 and VGT2 for one particular date (VGT1: 12/01/2001; VGT2: 30/09/2009) are shown in Fig. 2. Positive relative differences indicate $g_{i,C3} > g_{i,C2}$, resulting in lower $L_{TOA,i}$ with unchanged absolute calibration coefficients. In C3, the smile effect, which was especially present in the Blue band, is corrected for. For g_{SWIR} of both VGT1 and VGT2 there is no change, only in dark current (caused by thermally generated electrons that build up in the pixels) correction. Overall, the changes in equalization are larger for VGT2 (up to 1.5%) than for VGT1 (< 1%).

2.2. Sun-Earth distance modelling

In all previous versions of the SPOT/VGT processing chain, a bug

was present in the Sun-Earth distance modelling, which is corrected for in C3. In C2, in the calculation of the TOA reflectance, a fixed date (i.e. January 1st) was used instead of the actual date of acquisition. The corrected implementation of the solar illumination standardization results in a seasonal change in the TOA reflectances, with maximum difference (7%) on July 1st and no change on January 1st (Fig. 3). The effect of the correct modelling is thus identical from one year to the next and affects both instruments and all spectral bands in the same way.
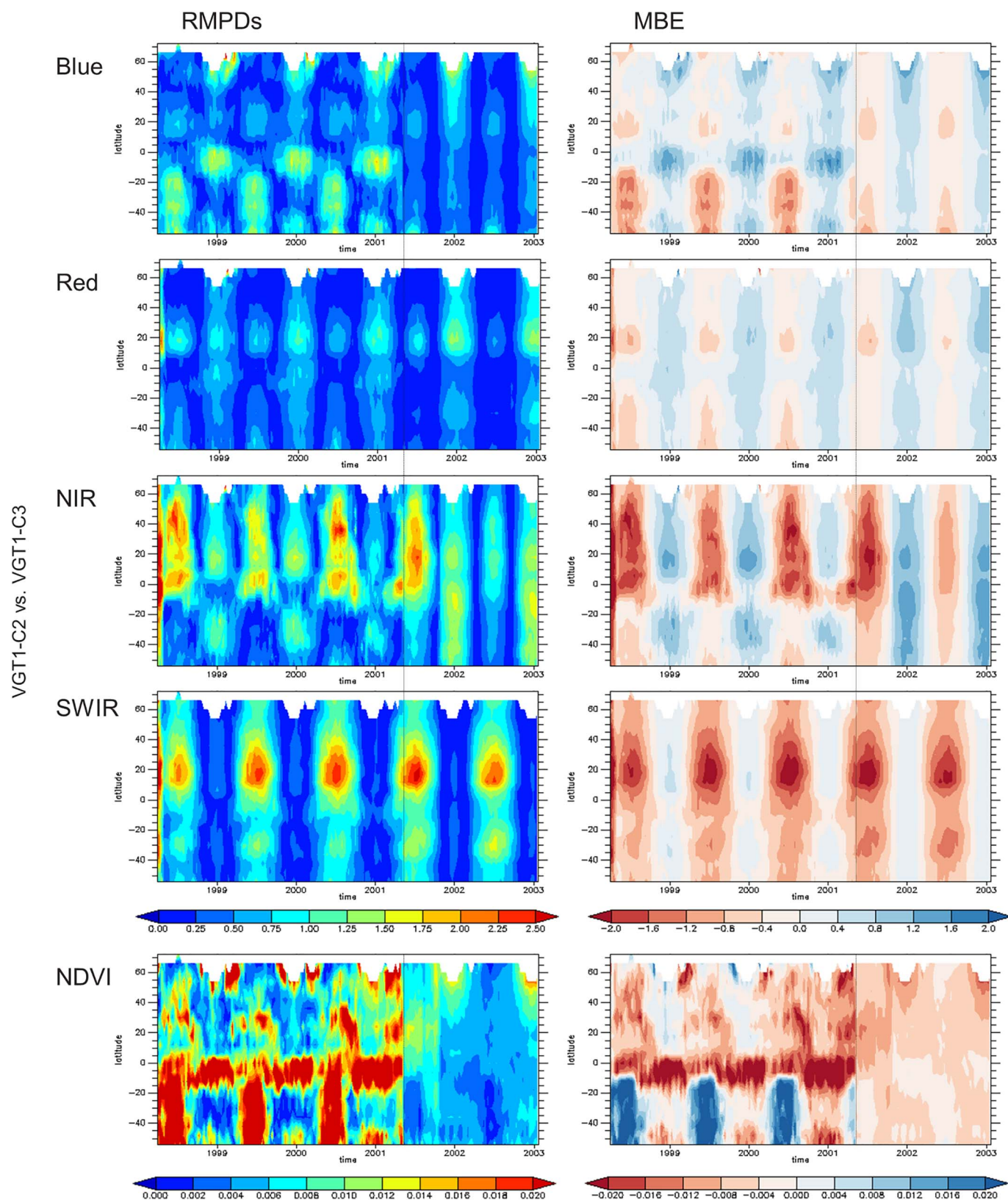
Fig. 5. Hovmöller diagrams of the RMPDs (left) and MBE (right, C2 minus C3) between the VGT1-C2 and VGT1-C3 reflectance bands (in %) and NDVI (unitless) (April/1998–January/2003). The dashed line highlights 11 May 2001, the date of change in the AOD retrieval in VGT1-C2.

2.3. Cloud, cloud shadow and snow/ice detection

Cloud and snow/ice detection are based on a number of reflectance threshold tests. In VGT-C2, the cloud and snow/ice detection changed from V1 to V2 on 11 May 2001 (Lissens et al., 2000; Wolters et al., 2016). Although this change resulted in a larger amount of clouds detected, omission errors were still present in the detection, due to the lack of thermal information (Fensholt et al., 2006; Swinnen and

Table 3
Validation metrics calculated between VGT2-C2 and VGT2-C3 (February/2003–May/2014), using the 'All constraints' sampling scheme.

	a	b	R^2	RMSD	RMPDs	RMPDu	MBE
All dekads (N = 408)							
Blue	0.23	1.0244	0.9791	0.66	0.35	0.56	− 0.34
Red	0.01	1.0271	0.9975	0.54	0.35	0.42	− 0.27
NIR	− 0.09	1.0434	0.9914	1.28	0.99	0.82	− 0.92
SWIR	0.17	1.0268	0.9962	0.99	0.77	0.62	− 0.72
NDVI	− 0.0007	1.0011	0.9974	0.0127	0.0003	0.0127	0.0002
1st dekads of January (N = 11)							
Blue	− 0.13	0.9909	0.9949	0.35	0.19	0.30	0.18
Red	− 0.10	0.9970	0.9996	0.24	0.14	0.19	0.14
NIR	− 0.17	1.0013	0.9994	0.27	0.14	0.23	0.14
SWIR	− 0.11	1.0001	0.9998	0.18	0.10	0.15	0.10
NDVI	0.0028	0.9972	0.9991	0.0079	0.0018	0.0077	− 0.0017
1st dekads of July (N = 11)							
Blue	0.34	1.0896	0.9783	0.90	0.73	0.54	− 0.65
Red	− 0.03	1.0657	0.9985	0.73	0.67	0.29	− 0.47
NIR	− 0.24	1.0863	0.9967	1.98	1.92	0.46	− 1.80
SWIR	0.04	1.0678	0.9994	1.47	1.45	0.21	− 1.33
NDVI	− 0.0020	1.0039	0.9958	0.0157	0.0010	0.0156	− 0.0003

Veroustraete, 2008). In the VGT-C3 processing chain, the cloud and snow/ice detection was further improved by adding a number of decision rules to the existing V2 cloud and snow/ice detection schemes. Additional rules for cloud detection are derived from Quesney et al. (2003) and for snow/ice detection from Berthelot (2004), referred to as CLOUD V3 and SNOW/ICE V3. The detection scheme as described in the VGT-C3 Products User Manual (Wolters et al., 2016) results in around 6% more pixels detected as cloud or cloud shadow compared to VGT-C2 (Toté et al., 2016).

2.4. Tropospherical aerosol input for the atmospheric correction

Atmospheric corrections are based on the SMAC algorithm (Rahman and Dedieu, 1994), correcting for molecular and aerosol scattering, water vapour, ozone and other gaseous absorption. In VGT-C2, since 11 May 2001, the input of aerosol optical depth (AOD) for the atmospheric correction is, for pixels complying to a number of criteria, estimated from the Blue band and the NDVI through an optimization process (Maisongrande et al., 2004; Wolters et al., 2016). In VGT-C3, this method is applied on the entire series. Prior to 11 May 2001 (in VGT-C2) and for pixels not complying the criteria (in both VGT-C2 and VGT-C3), a time invariant function of latitude is used. The change results in a more realistic aerosol input for the entire C3 archive.

3. Materials and methods

3.1. Data used

3.1.1. SPOT-VEGETATION archive: Collection 2 and Collection 3

The entire archives (VGT-C2 and VGT-C3) of both VGT1 and VGT2 10-daily maximum NDVI syntheses (S10) of Top-Of-Canopy (TOC) reflectance and NDVI at 1/112° spatial resolution were considered for the evaluation. C2 consisted of VGT1 data from April/1998 until January/2003 and VGT2 data from February/2003 until May/2014. The reprocessing was however performed on the entire set of VGT1 and VGT2 acquisitions, resulting in a larger C3 dataset compared to C2 with availability of VGT1-C3 after February/2003, although in certain periods these synthesis products do not cover the entire globe. Fig. 4 (top) summarizes the data completeness over land (i.e. percentage land pixels not labelled as missing, cloud, shadow or snow) for S10 products over the period April/1998–May/2014. The seasonal pattern is caused by a relatively larger amount of missing observations due to illumination conditions or bad quality (as indicated by the status map) in the

Northern hemisphere winter. In general, in C3 there are around 5% fewer clear observations, resulting from a larger amount of clouds and shadows detected by the new detection method (see Section 2.3). For VGT1, the difference between C2 and C3 is larger before May/2001, the date where a different cloud and snow detection method was introduced.

Fig. 4 (middle) shows the equator local overpass times of SPOT4 (1998–2012) and SPOT5 (2002–2014). The SPOT satellites have a local equator-crossing time of around 10:30. According to the mission specifications, the orbital drift should be limited to 20 min (deviation from 10:30) in order to limit the Solar Zenith Angle (SZA) drift to 3° (Swinnen et al., 2014). SPOT4 overpass time was beyond user requirements as from November/2010. For SPOT5 this was the case from March/2013 onwards. The prolonged operation of VGT2 was decided in order to maximize the overlap with its successor PROBA-V. Swinnen et al. (2014) analysed the impact on the data quality and concluded that the impact of an overpass time deviation of 40 min is small.

3.1.2. METOP/AVHRR

The European Organisation for the Exploitation of Meteorological Satellites (EUMETSAT) operates the METOP-satellites, a series of polar orbiting meteorological satellites which form the space segment component of the overall EUMETSAT Polar System (EPS). METOP carries the AVHRR-instrument and has a stable equator local overpass time at around 8:20. The NDVI from METOP/AVHRR is provided by the LSA-SAF (http://landsaf.meteo.pt). Although not distributed by the LSA-SAF, the spectral bands Red (band 1), NIR (band 2) and SWIR (band 3A) are also used in the evaluation. The AVHRR S10 TOC surface reflectance and NDVI are processed in a very similar way to those of SPOT-VGT, with the same water vapour and ozone inputs, the same time invariant AOD latitude-function (here applied on all pixels) for atmospheric correction, and a similar compositing method (Eerens et al., 2009). Nevertheless, there are differences in calibration, cloud detection and overpass time stability, which makes the intercomparison with SPOT-VGT so useful. Global data from METOP-A (launched in 2006) for the period January/2008–May/2014 are used in the comparison.

3.1.3. TERRA/MODIS NDVI

The Moderate Resolution Imaging Spectroradiometer (MODIS) is mounted on two platforms, EOS-TERRA and AQUA. TERRA/MODIS has a morning equator overpass at around 10:30 local time, and captures data in 36 bands with a spatial resolution of 250 m (2 bands), 500 m (5 bands) and 1 km (29 bands). The NDVI is provided to the user in the form of 16-day or monthly composites at various resolutions. The data that are used in this study are the MOD13A3 Collection 5 data set, which is the TERRA/MODIS global monthly gridded NDVI at 1 km resolution, available from February/2000. Monthly data are used because the NDVI is provided to users in a 16-day or monthly composite, and no 10-daily composites are distributed. The data are weighted temporal averages and are normalized for viewing and illumination angles using the simple Walthall model (Walthall et al., 1985) to normalize the reflectance data to nadir and compute nadir-based VIS reflectances. The period February/2000–May/2014 is used. Maximum NDVI compositing is applied to adapt the temporal resolution of VGT-C2 and VGT-C3 to monthly syntheses.

3.1.4. Periods for intercomparison

The periods used for intercomparison are highlighted in Fig. 4 (bottom). The comparison between C2 and C3 is based on the time series April/1998–January/2003 for VGT1 (174 dekads), February/2003–May/2014 for VGT2 (408 dekads). Also, in order to evaluate the influence of the corrected Sun-Earth distance modelling, only respectively the 1st dekads of January and the 1st dekads of July were considered, reducing the amount of dekads in the analysis to 5 (for VGT1) and 11 (for VGT2). Next, the intercomparison between VGT1-C3 and
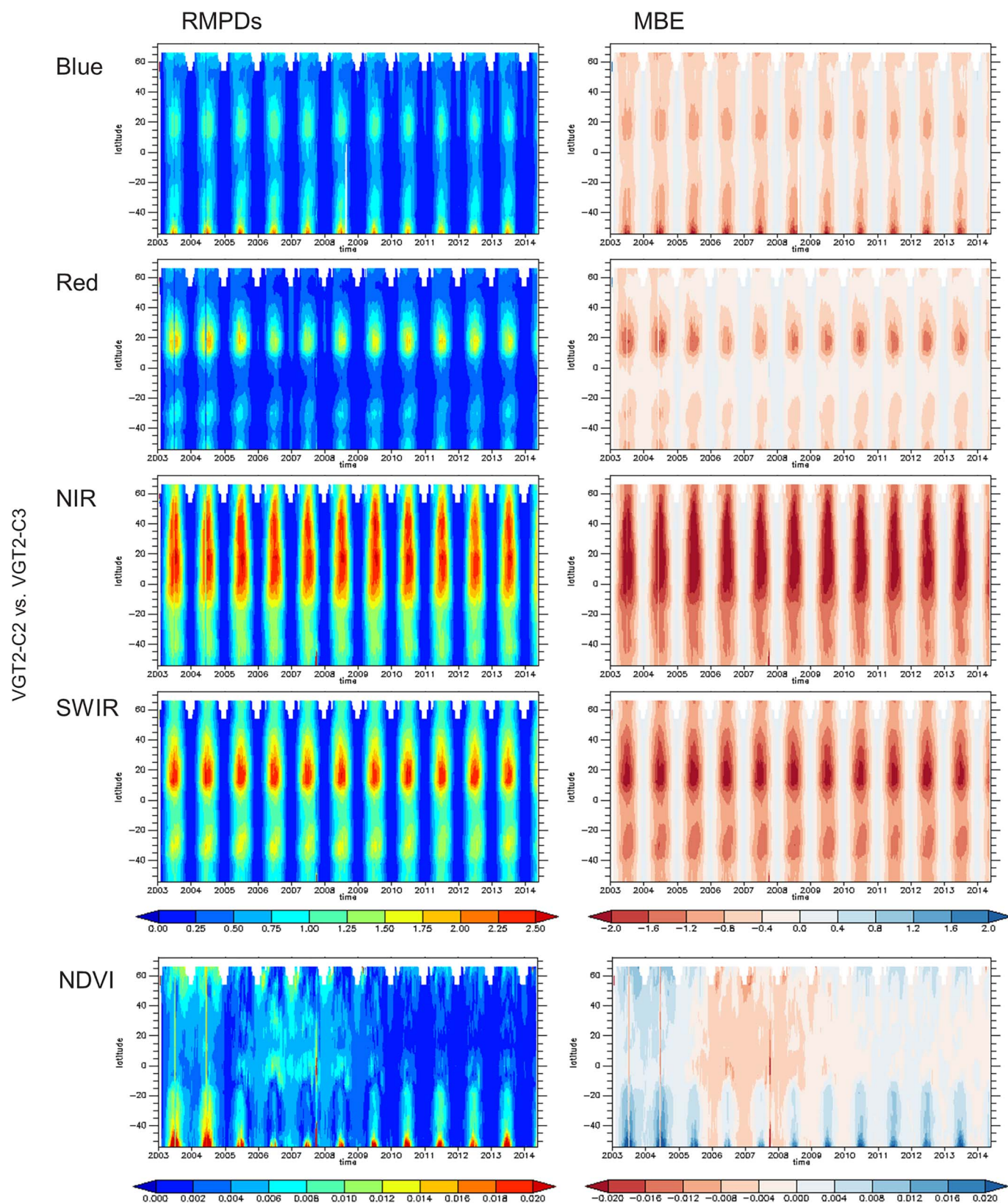
Fig. 6. Hovmöller diagrams of the RMPDs (left) and MBE (right, C2 minus C3) between the VGT2-C2 and VGT2-C3 reflectance bands (in %) and NDVI (unitless) (February/2003–May/2014).

VGT2-C3 is based on the time series April/2004–April/2007 (111 dekads): for this period (near) global coverage is available for both sensors and SPOT4 and SPOT5 have about the same equatorial local overpass time, with time differences below 5 min (Fig. 4, middle). Finally, for the consistency analysis between VGT-C3 and external datasets, intercomparison is done with METOP/AVHRR for the period January/2008–May/2014 (231 dekads) and with TERRA/MODIS for the period February/2000–May/2014 (172 months).

Table 4
Validation metrics calculated between VGT1-C3 and VGT2-C3 (April/2004–April/2007), using the 'Limited' sampling scheme.

	a	b	R^2	RMSD	RMPDs	RMPDu	MBE
All dekads (N = 111)							
Blue	0.17	0.9887	0.8249	1.98	0.12	1.98	− 0.10
Red	0.47	0.9920	0.9662	2.06	0.39	2.02	− 0.38
NIR	− 0.27	1.0020	0.9206	3.00	0.22	2.99	0.22
SWIR	− 0.18	1.0152	0.9724	2.81	0.24	2.80	− 0.16
NDVI	− 0.0057	0.9632	0.9652	0.0558	0.0246	0.0500	0.0224

3.2. Sampling

The global images are systematically spatially subsampled by taking the central pixel in each window of 21 by 21 pixels. This subsample is representative for the global patterns of vegetation and considerably reduces processing time, while retaining the relation between the observation and its viewing and illumination geometry.

Furthermore, a number of constraints are used to define additional comparison strategies: (i) consider only clear observations that are not identified as cloud/shadow/snow/unreliable in the status map that is delivered with the product; (ii) use only observations that are based on the identical day of observation (in the 10-daily compositing period) as identified through the time grid; (iii) consider close to nadir observations with VZA < 30°; (iv) use only observations that are both in either back or forward scatter direction. The 'All constraints' sampling scheme uses all 4 constraints, in order to retain a selection of clear observations of the same day, with an 'as similar as possible' observation geometry. This sampling scheme is used for the comparison between VGT-C2 and VGT-C3. In the comparison of VGT1 against VGT2, however, the constraint based on the identical day of observation could not be retained, because then too few pixels (only located in boreal areas) would remain to perform a statistically sound comparison. This results from the orbits of SPOT4 and SPOT5 not being aligned. In this case, a 'Limited' sampling scheme is used (Table 1). For the comparison to external datasets, only the first constraint is applied: the so-called 'Status Map' sampling scheme. Table 1 summarizes the different sets of constraints that were used in the different sampling schemes.

3.3. Validation metrics

The geometric mean regression (GMR) model, i.e. an orthogonal regression model, is used to identify the relationship between two data sets of remote sensing measurements, because both data sets are subject to noise (Ji and Gallo, 2006). The GMR model minimizes the sum of the products of the vertical and horizontal distances (errors on Y and X) and is of the form $Y = a + b \cdot X$, with slope $b = sign(R)\frac{\sigma_Y}{\sigma_X}$, intercept $a = \overline{Y} - b \cdot \overline{X}$, with σ_X and σ_Y the standard deviations of X and Y, R the correlation coefficient, and sign() the signum function that takes the sign of the variable between the brackets.

The coefficient of determination (R^2) indicates agreement or covariation between two data sets with respect to a linear regression model, summarizing the total data variation explained by this linear regression model.

$$R^2 = \left(\frac{\sigma_{X,Y}}{\sigma_X \bullet \sigma_Y}\right)^2 \tag{5}$$

with $\sigma_{X,Y}$ the co-variation of X and Y.

The Root Mean Squared Difference (RMSD) measures how far the difference between the two data sets deviates from 0 and is defined as:

$$RMSD = \sqrt{\frac{1}{n}\sum_{i=1}^{n}(X_i - Y_i)^2} \tag{6}$$

The RMSD expresses the overall difference, including random and

systematic differences, in the same unit as the datasets themselves, i.e. % (TOC reflectance) or unitless (NDVI). The random and systematic differences are derived from the mean squared difference (MSD), defined as:

$$MSD = \frac{1}{n}\sum_{i=1}^{n}(X_i - Y_i)^2 \tag{7}$$

The MSD is further partitioned into the systematic mean product difference (MPD_s) and the unsystematic or random mean product difference (MPD_u), i.e. how much of the difference between X and Y is not 'explained' by the GMR model (Willmott, 1981). In order to be comparable to the RMSD in terms of magnitude, the root of the systematic and unsystematic mean product difference is used ($RMPD_s$ and $RMPD_u$):

$$RMPD_u = \sqrt{MPD_u} = \sqrt{\frac{1}{n}\sum_{i=1}^{n}(|X_i - \widehat{X_i}|)(|Y_i - \widehat{Y_i}|)} \tag{8}$$

with $\widehat{X_i}$ and $\widehat{Y_i}$ estimated using the GMR model fit and n the number of samples. Then,

$$RMPD_s = \sqrt{MSD - MPD_u} \tag{9}$$

The partitioning of the difference into systematic and unsystematic difference provides additional information to the RMSD on the nature of the difference between two data sets.

The Mean Bias Error (MBE) measures the average actual difference between two data sets and positive and negative differences between observations, and is defined as:

$$MBE = \frac{1}{n}\sum_{i=1}^{n}(X_i - Y_i) = \overline{X} - \overline{Y} \tag{10}$$

Although the MBE is not the best way to estimate the bias, it is used here because it retains the sign of the difference between the data sets, unlike the other metrics.

3.4. Hovmöller diagrams

Hovmöller diagrams are used to perform a combined assessment of the spatial and temporal variability of the validation metrics as described above. The metrics are derived for each time step (10-day period or month) and for each spatial subset, defined as latitude bands of 6° wide, thereby depicting the temporal evolution of the spatial agreement (Meroni et al., 2013). The resulting time-latitude Hovmöller diagram allows summarizing the space-time features of the time series evaluation.

4. Results and discussion

4.1. Comparison between VGT-C2 and VGT-C3

In order to provide users insights in the differences caused by the reprocessing, the C2 and C3 archives are compared, separately for VGT1 and VGT2.

4.1.1. VGT1

The results of the GMR between VGT1-C2 and VGT1-C3 using the 'All constraints' sampling scheme are summarized in Table 2. For the spectral bands, the results of the GMR show a close to linear relationship (R^2 close to 1). Overall, surface reflectances for NIR (RMSD = 1.2%) and SWIR (RMSD = 1.1%) bands are slightly higher after the reprocessing, resulting in a negative MBE. For surface reflectance, there is a slight difference in the bias between January and July, resulting from the corrected Sun-Earth distance modelling: regression line slopes are below 1 for January (i.e. VGT1-C3 < VGT1-C2), and above 1 for July (i.e. VGT1-C3 > VGT1-C2). This is also reflected in the MBE. Systematic differences are largest for NIR and SWIR
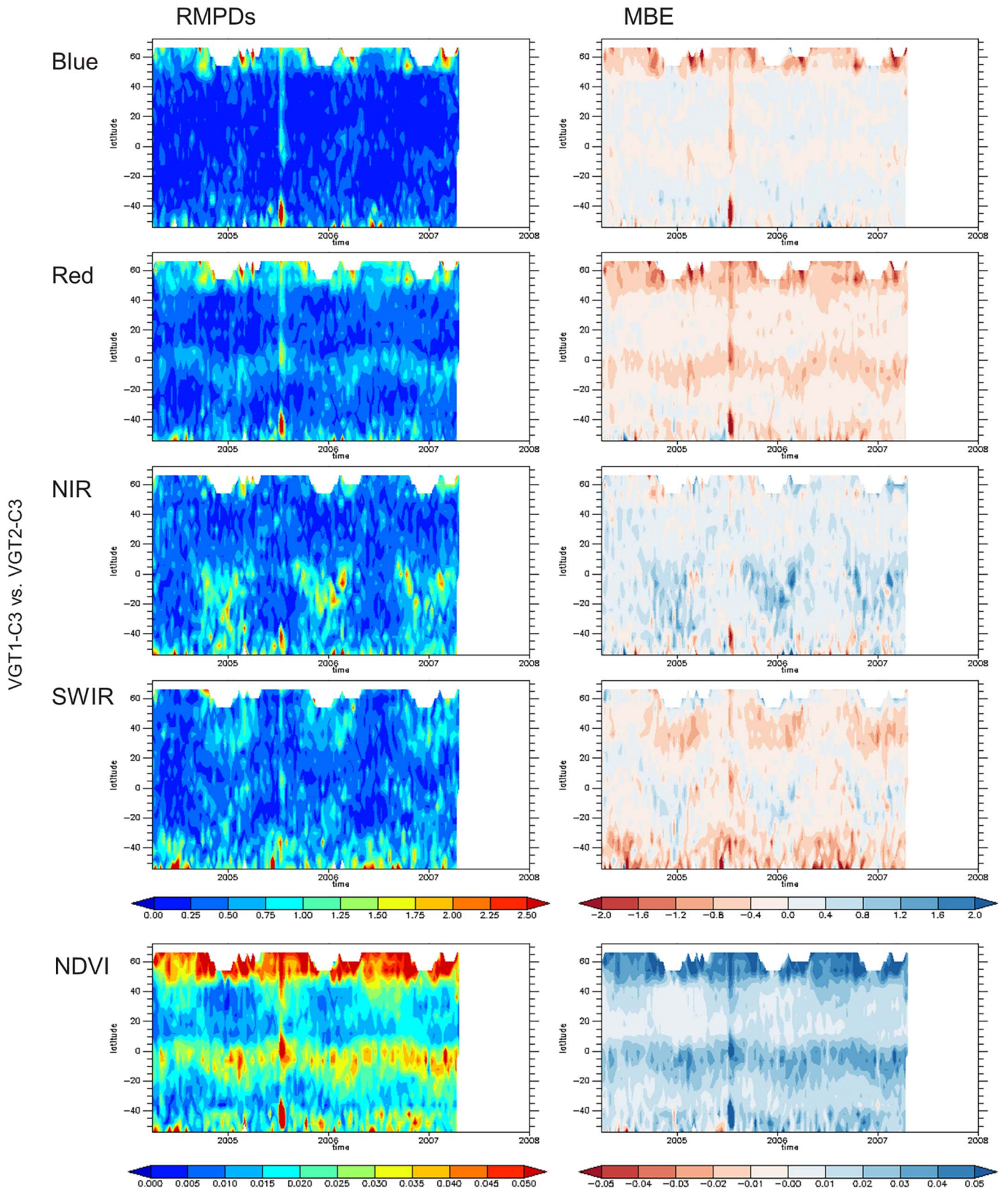
Fig. 7. Hovmöller diagrams of the RMPDs (left) and MBE (right, VGT2 minus VGT1) between the VGT1-C3 and VGT2-C3 reflectance bands (in %) and NDVI (unitless) (April/2004–April/2007).

in July (above 1%). For the NDVI, both the overall, January and July GMR lines are close to the 1:1 line. The validation metrics indicate that the overall impact of the reprocessing on the NDVI is relatively small.

The spatio-temporal evolution of the difference between VGT1-C2 and VGT1-C3 surface reflectance and NDVI is evaluated through Hovmöller diagrams (Fig. 5). The changes to the AOD estimation that were implemented from 11 May 2001 onwards in the C2 archive (and applied in the full C3 archive) result in a larger difference before that
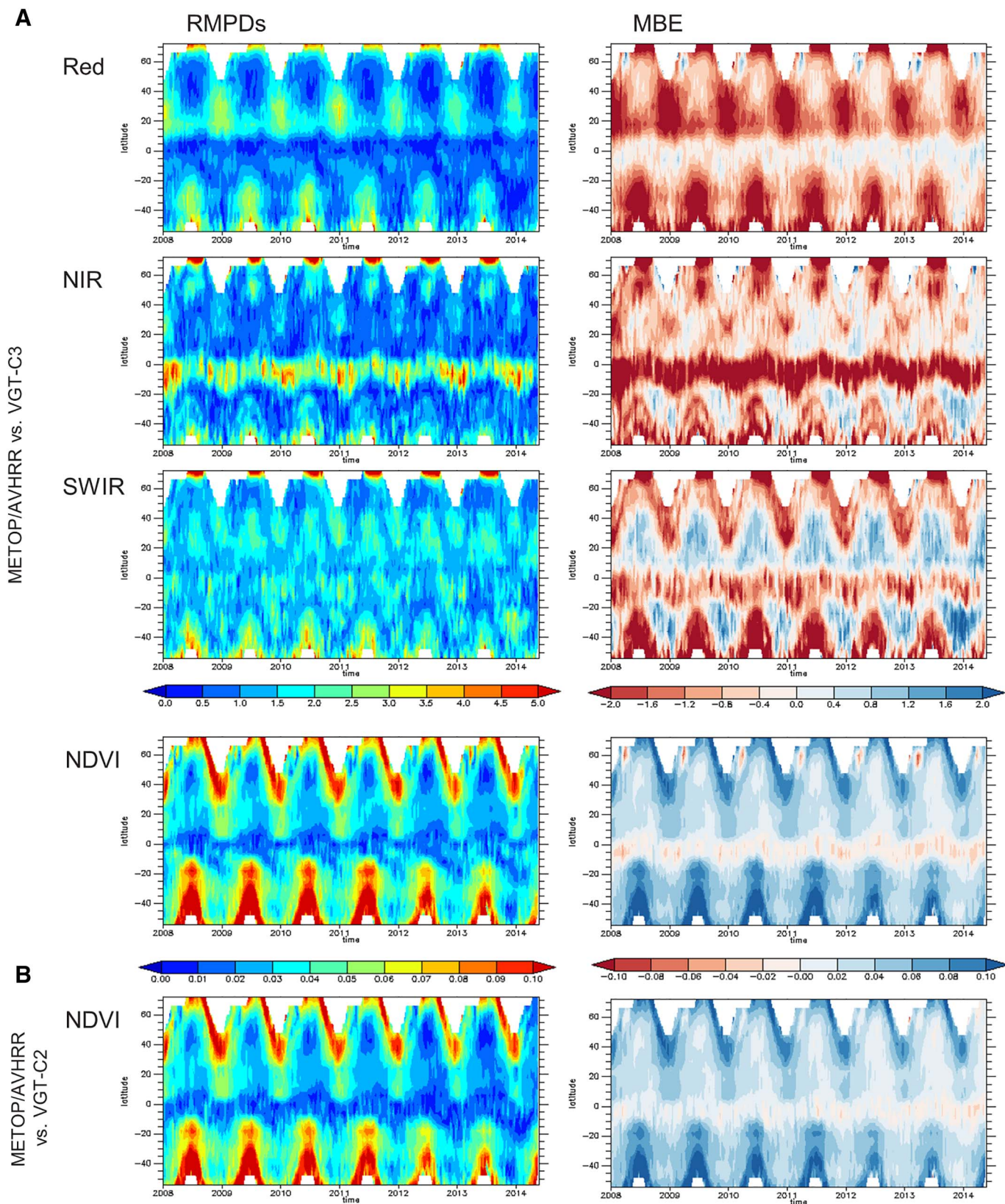
Fig. 8. Hovmöller diagrams of the RMPDs and MBE (METOP/AVHRR minus VGT2) between A. the surface reflectance bands (in %) and NDVI (unitless) derived from METOP/AVHRR and VGT2-C3, and B. NDVI derived from METOP/AVHRR and VGT2-C2, (January/2008–May/2014).

date. The impact is largest for Blue, NIR and the NDVI. The seasonal patterns, with largest differences in July and smallest differences in January, are related to the Sun-Earth distance correction. The effect is most visible for NIR and SWIR, and more pronounced in the Northern

hemisphere, due to higher reflectances in the vegetative season.

4.1.2. VGT2

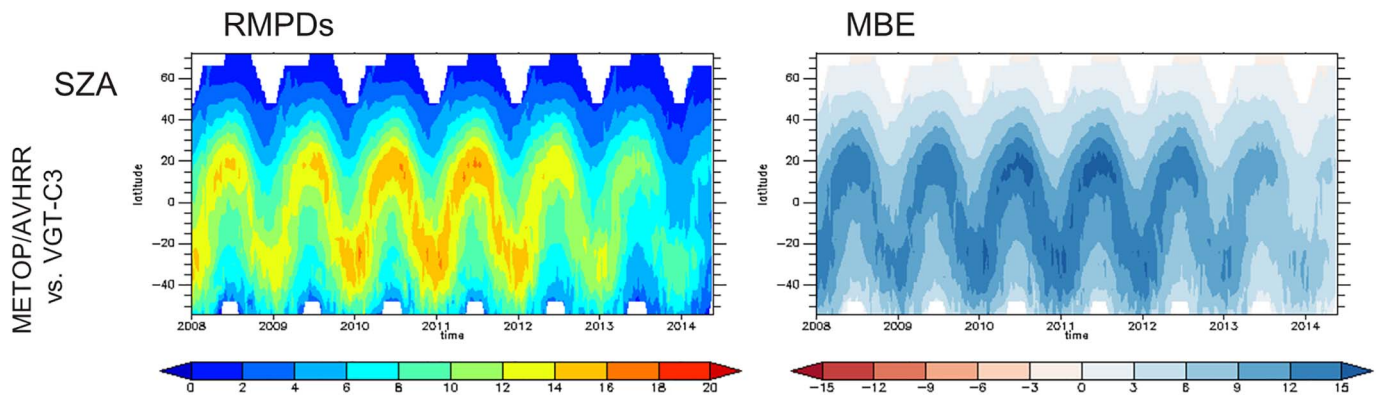Similar to VGT1, the results of the GMR between VGT2-C2 and

Fig. 9. Hovmöller diagrams of the RMPDs and MBE (METOP/AVHRR minus VGT2) between the SZA (in °) from METOP/AVHRR and VGT2-C3 (January/2008–May/2014).

VGT2-C3 show a close to linear relationship for all spectral bands and the NDVI (Table 3). Surface reflectances are overall slightly higher after the reprocessing. The impact is larger on NIR (RMSD = 1.3%) and SWIR (RMSD = 1.0%), smaller on Blue (RMSD = 0.7%) and Red (RMSD = 0.5%). GMR lines are close to the 1:1 line for January, but deviations are larger for July, originating from the corrected Sun-Earth distance modelling. This is also reflected in the other metrics: in general, the bias is very small in January, while the 1st dekads of July clearly show a larger, negative bias (VGT2-C3 > VGT2-C2). The seasonal difference is the largest for NIR and SWIR, smaller for Blue and Red, and negligible for the NDVI. The metrics based on the overall comparison of the NDVI show that the impact of the reprocessing is small.

Fig. 6 shows the Hovmöller diagrams of the systematic difference and mean bias between VGT2-C2 and VGT2-C3 surface reflectance and NDVI. Seasonal patterns, mostly visible in NIR and SWIR are caused by the Sun-Earth distance correction, similar to Fig. 5. Trends over the years due to changes in calibration coefficients are visible, especially for Blue (increasing MBE due to increasing A_i) and Red (fluctuating lower/higher MBE due to lower/higher A_i). For the NDVI, differences over the years are caused by changes in the Red calibration: for 2003–2005 the VGT2-C3 NDVI is slightly lower (−0.008), for 2006–2008 the VGT2-C3 NDVI is slightly higher (+0.004).

For a few dates, the differences between VGT2-C2 and VGT2-C3 are notably higher. For the 1st dekad of July/2003 and the 2nd dekad of June/2004, analysis revealed issues in the VGT2-C2 archive. The period October–November/2007 suffered from geolocation errors in VGT2-C2, resulting in a number of segments not being used in the dekadal compositing. These problems were fixed in VGT2-C3.

4.2. Consistency analysis between VGT1 and VGT2

The consistency analysis between VGT1 and VGT2 is based on a time period where both SPOT4 and SPOT5 have about the same equatorial local overpass time (see Section 3.1.1) and there is thus limited difference in illumination conditions. Although the absolute calibration factors were updated in C3 for both sensors, and VGT1 and VGT2 were intercalibrated, there are other factors that can influence the consistency between the observed reflectance values: (i) small differences in spectral response functions (Fensholt et al., 2009), with non-linear impact on the NDVI (Trishchenko et al., 2002); and (ii) non-alignment of the orbits of SPOT4 and SPOT5, causing opposite viewing angles for the same registration day.

The results of the GMR between VGT1-C3 and VGT2-C3 using the 'Limited' sampling scheme are summarized in Table 4. GMR lines show intercepts close to 0 and slopes very close to 1 for all spectral bands. VGT2 surface reflectance is slightly lower than VGT1 surface reflectance (i.e. MBE is negative) for Blue (RMSD = 2.0%), Red (RMSD = 2.1%) and SWIR (RMSD = 2.8%). The opposite is true for

NIR (RMSD = 3.0%). Both the mean and systematic bias remain however well below 1%.

For the NDVI, the GMR slope is below 1, indicating that VGT2 NDVI is higher than the VGT1 NDVI (MBE = 0.02, RMSD = 0.06) and that differences increase with higher NDVI.

For surface reflectance, there is no spatio-temporal pattern in the bias (Fig. 7), except for outliers for the 2nd dekad of July/2005. This is caused by a number of missing segments in the VGT1 acquisitions. In contrast, the NDVI shows a larger bias (VGT2 > VGT1) in the tropics and in the Northern hemisphere boreal areas. This is possibly resulting from bidirectional (in this case viewing geometry) effects on the NDVI (Gao et al., 2002): boreal forests are severely affected by viewing geometry, and in tropical forests bidirectional effects are large compared to the small seasonal cycle in the NDVI (Los et al., 2005).

4.3. Comparison to METOP/AVHRR surface reflectance and NDVI

In the previous sections, we discussed the impact of the reprocessing on the SPOT/VGT archive, and its effect on the consistency of the combined SPOT/VGT time series from two sensors. In the following sections, the C3 archive is compared to external datasets. Although there are intrinsic differences between datasets derived from different sensors (linked to differences in spectral response functions, calibration, processing, etc.), it is interesting to evaluate the temporal stability of the differences.

The systematic bias between VGT2-C3 and METOP/AVHRR shows a small decreasing trend for Red, NIR and SWIR (Fig. 8A): from 2012 onwards, the MBE evolves to values closer to 0 overall (Red) and more specifically in the Northern hemisphere (NIR and SWIR), or to more positive values in the Southern hemisphere (NIR and SWIR). Also the NDVI shows a slight decrease in RMPDs and MBE, indicating a relative gradual increase in the VGT2 NDVI. In comparison with the MBE between VGT2-C2 and METOP/AVHRR (Fig. 8B) however, the differences between sensors are more stable over time after the reprocessing.

The trends that are still visible after the reprocessing are consistent with the change in overpass time of SPOT5 (Fig. 4, middle), evolving towards smaller time differences with the overpass time of METOP/AVHRR, and the associated change in illumination conditions. Fig. 9 shows the RMPDs and MBE between the SZA of METOP/AVHRR and VGT2: with the shift to earlier overpass time of SPOT5 from 2012 onwards, and thus increasing SZA of the SPOT5 acquisitions, the difference in SZA between the two sensors decreases. TOC NDVI is known to increase with an increase in SZA (Deering et al., 1999), because a higher fraction of solar radiation is intercepted by the vegetation canopy (Nagol et al., 2014). This is especially the case for observations with initial high SZAs, e.g. at higher latitudes, and the effect is larger on Red than on NIR (Hagolle, 2007), hence the increase in NDVI. The sensitivity of TOC NDVI to changes in SZA will however decrease with increasing vegetation density (Kaufmann et al., 2000).
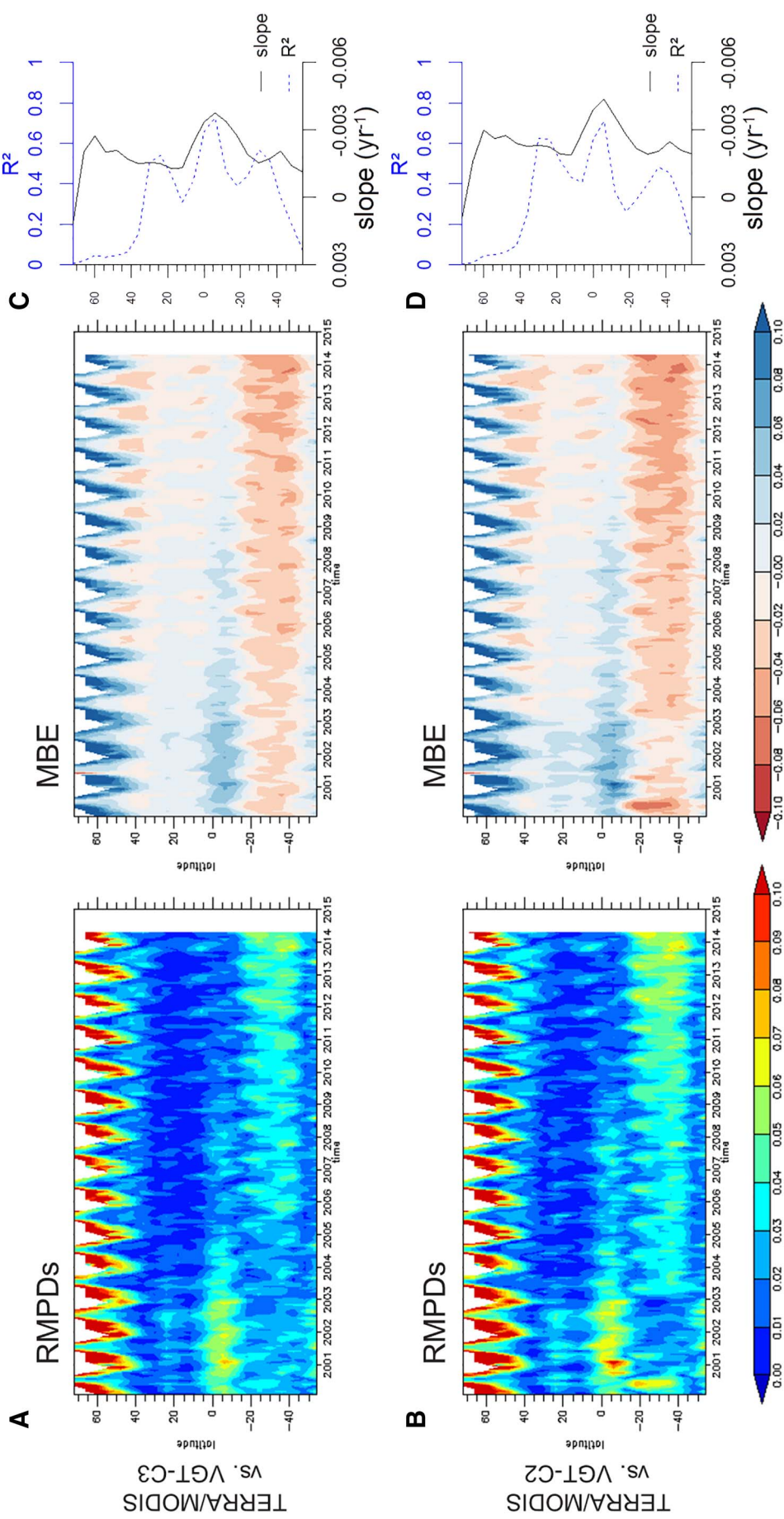
Fig. 10. Hovmöller diagrams of the RMPDs and MBE (TERRA/MODIS minus VGT) between the NDVI (unitless) derived from A. TERRA/MODIS and VGT-C3, and B. TERRA/MODIS and VGT-C2, (February/2000–May/2014). C. and D. Slope (yr^{-1}) and R^2 of the linear trend in MBE.

4.4. Comparison to TERRA/MODIS NDVI

The spatio-temporal evolution of the RMPDs and MBE between monthly NDVI of VGT-C3 and TERRA/MODIS is shown in Fig. 10A. As in VGT-C2 (Fig. 4), also in VGT-C3 the switch from VGT1 to VGT2 is made in February/2003. The Hovmöller plots indicate slightly higher RMPDs for the comparison between VGT1 and MODIS, especially in the tropics, where MODIS NDVI is higher than VGT1 NDVI. The jump towards somewhat higher NDVI values with the switch from VGT1 to VGT2, as reported by e.g. Fensholt et al. (2009) based on analysis on C2, and clearly visible in Fig. 10B, is thus not completely accounted for in C3.

The Hovmöller plots in Fig. 10 also show an increasing bias between VGT2 and MODIS, starting from 2008, but more pronounced from 2012 onwards. The MBE between VGT2-C3 and MODIS (Fig. 10A) evolves to more negative values at a rate of up to $-0.004\,\mathrm{yr}^{-1}$ (Fig. 10C), indicating VGT2 NDVI gradually evolved to slightly higher values compared to MODIS NDVI. This is in agreement with the results of Section 4.3: a small increase in NDVI caused by shifts towards higher SZA. The trends are however smaller compared to the analysis on VGT2-C2 and MODIS (Fig. 10D). Also, the trends could be the result of a combined effect, since it is to be noted that MODIS NDVI has been reported to show an opposite trend with declining NDVI at a rate of $0.001–0.004\,\mathrm{yr}^{-1}$, related to sensor degradation of the Blue, Red and NIR bands (Tian et al., 2015; Wang et al., 2012). Recent improvements made in MODIS Collection 6, have been reported to have removed all known calibration drifts (Doelling et al., 2015).

5. Conclusions

The aim of this paper is to inform the user community of the modifications in the SPOT/VEGETATION processing chain, and the impacts on the new VGT-C3 archive. The evaluation of the reprocessing is based on (i) the relative comparison between VGT-C2 and VGT-C3 TOC-S10 surface reflectances and NDVI, (ii) consistency analysis between VGT1-C3 and VGT2-C3, and (iii) the comparison of the archive with external datasets from METOP/AVHRR and TERRA/MODIS.

Overall, surface reflectances are slightly higher after the reprocessing, for both VGT1 (RMSD between 0.5% and 1.6%) and VGT2 (RMSD between 0.2% and 2.0%), with larger differences in July compared to January, caused by the corrected Sun-Earth distance modelling. For NDVI, the overall impact of the reprocessing is relatively small (RMSD < 0.02) and there are no seasonal fluctuations. Trends in this difference over the years are related to changes in calibration coefficients. The changes to the atmospheric correction that were implemented from 11 May 2001 onwards in the VGT1-C2 archive (and applied in the full C3 archive) result in a larger bias before that date.

VGT1 and VGT2 surface reflectance consistency is very high, with overall both the mean and systematic bias remaining below 0.4% and the RMSD below 3%. VGT2 surface reflectance is slightly lower than VGT1 surface reflectance (i.e. negative MBE) for Blue (RMSD = 2.0%), Red (RMSD = 2.1%) and SWIR (RMSD = 2.8%). The opposite is true for NIR (RMSD = 3.0%). The magnitude of the bias between VGT1 and VGT2 is the largest for the NIR band and the NDVI (VGT2 > VGT1, especially for higher NDVI values). The NDVI shows largest bias in the tropics and in the Northern hemisphere boreal areas, possibly due to bidirectional effects caused by differences in viewing geometry.

Both the comparison with METOP/AVHRR (surface reflectance and NDVI) and TERRA/MODIS (NDVI) reveal trends over time. Between VGT2 and METOP/AVHRR, all three bands (Red, NIR and SWIR) show a trend of decreasing systematic bias, starting roughly from 2012. Also the NDVI shows decreasing RMPDs and MBE from 2012 onwards, indicating a gradually higher VGT2 NDVI. The comparison with TERRA/MODIS reveals an increasing bias between VGT2 and MODIS at an average rate of up to $0.004\,\mathrm{yr}^{-1}$. VGT2 NDVI seems to be gradually evolving to slightly larger values compared to MODIS NDVI, a trend

that is consistent with the change in overpass time of VGT2 and the different illumination conditions caused by the orbital drift. TERRA/MODIS NDVI has however been reported to have declining NDVI at a rate of $0.001–0.004\,\mathrm{yr}^{-1}$, due to sensor degradation of Blue, Red and NIR bands (Tian et al., 2015; Wang et al., 2012). Whether METOP-AVHRR suffers or not from sensor degradation is not clear. Results demonstrate the SPOT/VGT-C3 archive is more stable over time compared to the previous archive, although bidirectional reflectance distribution function (BRDF) normalization is recommended in order to correct for bidirectional (illumination and viewing geometry) effects.

References

Atzberger, C., Eilers, P.H.C., 2011. A time series for monitoring vegetation activity and phenology at 10-daily time steps covering large parts of South America. Int. J. Digit. Earth 4, 365–386. http://dx.doi.org/10.1080/17538947.2010.505664.

Bartholomé, E., Belward, A.S., 2005. GLC2000: a new approach to global land cover mapping from Earth observation data. Int. J. Remote Sens. 26, 1959–1977. http://dx.doi.org/10.1080/01431160412331291297.

Bartholomé, E., Henry, P., Fierens, F., Eerens, H., 2006. Note to Users of VEGETATION Data: Problems with Radiometric Calibration of VEGETATION 2 Data.

Berthelot, B., 2004. Snow Detection on VEGETATION Data - Improvement of Cloud Screening. (No. NOV-3128-NT-2295, v1.1).

Boles, S.H., Xiao, X., Liu, J., Zhang, Q., Munkhtuya, S., Chen, S., Ojima, D., 2004. Land cover characterization of Temperate East Asia using multi-temporal VEGETATION sensor data. Remote Sens. Environ. 90, 477–489. http://dx.doi.org/10.1016/j.rse.2004.01.016.

Bouvet, M., 2014. Radiometric comparison of multispectral imagers over a pseudo-invariant calibration site using a reference radiometric model. Remote Sens. Environ. 140, 141–154. http://dx.doi.org/10.1016/j.rse.2013.08.039.

Carreiras, J.M.B., Pereira, J.M.C., Campagnolo, M.L., Shimabukuro, Y.E., 2006. Assessing the extent of agriculture/pasture and secondary succession forest in the Brazilian Legal Amazon using SPOT VEGETATION data. Remote Sens. Environ. 101, 283–298. http://dx.doi.org/10.1016/j.rse.2005.12.017.

Deering, D.W., Eck, T.F., Banerjee, B., 1999. Characterization of the reflectance anisotropy of three boreal forest canopies in spring-summer. Remote Sens. Environ. 67, 205–229. http://dx.doi.org/10.1016/S0034-4257(98)00087-X.

Delbart, N., Le Toan, T., Kergoat, L., Fedotova, V., 2006. Remote sensing of spring phenology in boreal regions: a free of snow-effect method using NOAA-AVHRR and SPOT-VGT data (1982-2004). Remote Sens. Environ. 101, 52–62. http://dx.doi.org/10.1016/j.rse.2005.11.012.

Deronde, B., Debruyn, W., Gontier, E., Goor, E., Jacobs, T., Verbeiren, S., Vereecken, J., 2014. 15 years of processing and dissemination of SPOT-VEGETATION products. Int. J. Remote Sens. 35, 2402–2420. http://dx.doi.org/10.1080/01431161.2014.883102.

Dierckx, W., Sterckx, S., Benhadj, I., Livens, S., Duhoux, G., Van Achteren, T., Francois, M., Mellab, K., Saint, G., 2014. PROBA-V mission for global vegetation monitoring: standard products and image quality. Int. J. Remote Sens. 35, 2589–2614. http://dx.doi.org/10.1080/01431161.2014.883097.

Doelling, D.R., Wu, A., Xiong, X., Scarino, B.R., Bhatt, R., Haney, C.O., Morstad, D., Gopalan, A., 2015. The radiometric stability and scaling of collection 6 terra- and aqua-MODIS VIS, NIR, and SWIR spectral bands. IEEE Trans. Geosci. Remote Sens. 53, 4520–4535. http://dx.doi.org/10.1109/TGRS.2015.2400928.

Durgun, Y., Gobin, A., Gilliams, S., Duveiller, G., Tychon, B., 2016. Testing the contribution of stress factors to improve wheat and maize yield estimations derived from remotely-sensed dry matter productivity. Remote Sens. 8, 170. http://dx.doi.org/10.3390/rs8030170.

Eerens, H., Baruth, B., Bydekerke, L., Deronde, B., Dries, J., Goor, E., Heyns, W., Jacobs, T., Ooms, B., Piccard, I., Royer, A., Swinnen, E., 2009. Ten-daily global composites of METOP-AVHRR. In: Proc. 6th Int. Symp. Digit. Earth, pp. 8–13. http://dx.doi.org/10.1117/12.873233.

Fensholt, R., Nielsen, T.T., Stisen, S., 2006. Evaluation of AVHRR PAL and GIMMS 10-day composite NDVI time series products using SPOT-4 vegetation data for the African continent. Int. J. Remote Sens. 27, 2719–2733. http://dx.doi.org/10.1080/01431160600567761.

Fensholt, R., Rasmussen, K., Nielsen, T.T., Mbow, C., 2009. Evaluation of earth observation based long term vegetation trends — intercomparing NDVI time series trend analysis consistency of Sahel from AVHRR GIMMS, Terra MODIS and SPOT VGT data. Remote Sens. Environ. 113, 1886–1898. http://dx.doi.org/10.1016/j.rse.2009.04.004.

Fougnie, B., Henry, P., Cabot, F., Meygret, A., Laubies, M.-C., 2000. VEGETATION: inflight multi-angular calibration. In: Proceedings of SPIE, pp. 331–338.

Fraser, R.H., Li, Z., 2002. Estimating fire-related parameters in boreal forest using SPOT VEGETATION. Remote Sens. Environ. 82, 95–110. http://dx.doi.org/10.1016/S0034-4257(02)00027-5.

Gao, F., Jin, Y., Li, X., Schaaf, C.B., Strahler, A.H., 2002. Bidirectional NDVI and atmospherically resistant BRDF inversion for vegetation canopy. IEEE Trans. Geosci. Remote Sens. 40, 1269–1278. http://dx.doi.org/10.1109/TGRS.2002.800241.

Goor, E., Dries, J., Daems, D., Paepen, M., Niro, F., Goryl, P., Mougnaud, P., Della Vecchia, A., 2016. PROBA-V mission exploitation platform. Remote Sens. 8, 564. http://dx.doi.org/10.3390/rs8070564.

Hagolle, O., 2007. Effet d'un changement d'heure de passage sur les séries temporelles de données de l'instrument VEGETATION. (No. DCT/SI/MO/2007 – 07315).

Henry, P., Meygret, A., 2001. Calibration of HRVIR and VEGETATION cameras on SPOT4. Adv. Sp. Res. 28, 49–58.

Immerzeel, W.W., Quiroz, R.A., De Jong, S.M., 2005. Understanding precipitation patterns and land use interaction in Tibet using harmonic analysis of SPOT VGT - S10 NDVI time series. Int. J. Remote Sens. 26, 2281–2296.

Ji, L., Gallo, K., 2006. An agreement coefficient for image comparison. Photogramm. Eng. Remote. Sens. 72, 823–833. http://dx.doi.org/10.14358/PERS.72.7.823.

Kamthonkiat, D., Honda, K., Turral, H., Tripathi, N.K., Wuwongse, V., 2005. Discrimination of irrigated and rainfed rice in a tropical agricultural system using SPOT VEGETATION NDVI and rainfall data. Int. J. Remote Sens. 26, 2527–2547. http://dx.doi.org/10.1080/01431160500104335.

Kaufmann, R.K., Zhou, L., Knyazikhin, Y., Shabanov, V., Myneni, R.B., Tucker, C.J., 2000. Effect of orbital drift and sensor changes on the time series of AVHRR vegetation index data. Geosci. Remote Sensing, IEEE Trans. Geosci. Remote Sens. 38, 2584–2597.

Lachérade, S., Fougnie, B., Henry, P., Gamet, P., 2013. Cross calibration over desert sites: description, methodology, and operational implementation. IEEE Trans. Geosci. Remote Sens. 51, 1098–1113. http://dx.doi.org/10.1109/TGRS.2012.2227061.

Lasaponara, R., 2006. Estimating spectral separability of satellite derived parameters for burned areas mapping in the Calabria region by using SPOT-vegetation data. Ecol. Model. 196, 265–270. http://dx.doi.org/10.1016/j.ecolmodel.2006.02.025.

Lhermitte, S., Verbesselt, J., Verstraeten, W.W., Coppin, P., 2011. A comparison of time series similarity measures for classification and change detection of ecosystem dynamics. Remote Sens. Environ. 115, 3129–3152. http://dx.doi.org/10.1016/j.rse.2011.06.020.

Lissens, G., Kempeneers, P., Fierens, F., Van Rensbergen, J., 2000. Development of cloud, snow, and shadow masking algorithms for VEGETATION imagery. In: Proceedings of IEEE IGARSS Taking the Pulse of the Planet: The Role of Remote Sensing in Managing the Environment, pp. 834–836 (doi:10.1109/IGARSS.2000.861719).

Los, S., North, P., Grey, W., Barnsley, M., 2005. A method to convert AVHRR normalized difference vegetation index time series to a standard viewing and illumination geometry. Remote Sens. Environ. 99, 400–411. http://dx.doi.org/10.1016/j.rse.2005.08.017.

Lupo, F., Reginster, I., Lambin, E.F., 2001. Monitoring land-cover changes in West Africa with SPOT vegetation: impact of natural disasters in 1998–1999. Int. J. Remote Sens. 22, 2633–2639. http://dx.doi.org/10.1080/01431160117700.

Maisongrande, P., Duchemin, B., Dedieu, G., 2004. VEGETATION/SPOT: an operational mission for the Earth monitoring; presentation of new standard products. Int. J. Remote Sens. 25, 9–14. http://dx.doi.org/10.1080/0143116031000115265.

Meroni, M., Atzberger, C., Vancutsem, C., Gobron, N., Baret, F., Lacaze, R., Eerens, H., Leo, O., 2013. Evaluation of agreement between space remote sensing SPOT-VEGETATION fAPAR time series. IEEE Trans. Geosci. Remote Sens. 51, 1951–1962. http://dx.doi.org/10.1109/TGRS.2012.2212447.

Nagol, J., Vermote, E., Prince, S., 2014. Quantification of impact of orbital drift on interannual trends in AVHRR NDVI data. Remote Sens. 6, 6680–6687. http://dx.doi.org/10.3390/rs6076680.

Passot, X., 2001. VEGETATION image processing methods in the CTIV. In: Proc. Veg. 2000 Conf.

Quesney, A., Bruniquel-Pinel, V., Bru, R., 2003. A Multisensor Generic Cloud Screening Toolbox. (No. NOV-3128-NT-1759, v1.0).

Rahman, H., Dedieu, G., 1994. SMAC: a simplified method for the atmospheric correction of satellite measurements in the solar spectrum. Int. J. Remote Sens. 15, 123–143. http://dx.doi.org/10.1080/01431169408954055.

Rembold, F., Atzberger, C., Savin, I., Rojas, O., 2013. Using low resolution satellite imagery for yield prediction and yield anomaly detection. Remote Sens. 5, 1704–1733. http://dx.doi.org/10.3390/rs5041704.

Sterckx, S., Livens, S., Adriaensen, S., 2013. Rayleigh, deep convective clouds, and cross-sensor desert vicarious calibration validation for the PROBA-V mission. IEEE Trans. Geosci. Remote Sens. 51, 1437–1452. http://dx.doi.org/10.1109/TGRS.2012.2236682.

Sterckx, S., Benhadj, I., Duhoux, G., Livens, S., Dierckx, W., Goor, E., Adriaensen, S., Heyns, W., Van Hoof, K., Strackx, G., Nackaerts, K., Reusen, I., Van Achteren, T., Dries, J., Van Roey, T., Mellab, K., Duca, R., Zender, J., 2014. The PROBA-V mission: image processing and calibration. Int. J. Remote Sens. 35, 2565–2588. http://dx.doi.org/10.1080/01431161.2014.883094.

Swinnen, E., Toté, C., 2017. Comparison Between SPOT-VGT and PROBA-V. (VITO Technical Report).

Swinnen, E., Veroustraete, F., 2008. Extending the SPOT-VEGETATION NDVI time series (1998–2006) back in time with NOAA-AVHRR data (1985–1998) for Southern Africa. IEEE Trans. Geosci. Remote Sens. 46, 558–572. http://dx.doi.org/10.1109/TGRS.2007.909948.

Swinnen, E., Verbeiren, S., Deronde, B., Henry, P., 2014. Assessment of the impact of the orbital drift of SPOT-VGT1 by comparison with SPOT-VGT2 data. Int. J. Remote Sens. 35, 2421–2439. http://dx.doi.org/10.1080/01431161.2014.883100.

Tansey, K., Grégoire, J.-M., Defourny, P., Leigh, R., Pekel, J.-F., van Bogaert, E., Bartholomé, E., 2008. A new, global, multi-annual (2000–2007) burnt area product at 1 km resolution. Geophys. Res. Lett. 35. http://dx.doi.org/10.1029/2007GL031567.

Tian, F., Fensholt, R., Verbesselt, J., Grogan, K., Horion, S., Wang, Y., 2015. Evaluating temporal consistency of long-term global NDVI datasets for trend analysis. Remote Sens. Environ. 2. http://dx.doi.org/10.1016/j.rse.2015.03.031.

Tonini, F., Lasinio, G.J., Hochmair, H.H., 2012. Mapping return levels of absolute NDVI variations for the assessment of drought risk in Ethiopia. Int. J. Appl. Earth Obs. Geoinf. 18, 564–572. http://dx.doi.org/10.1016/j.jag.2012.03.018.

Toté, C., Swinnen, E., Sterckx, S., 2016. Evaluation of the Re-processed VGT1 and VGT2 Archive - Final Report. (VITO Technical Report).

Trishchenko, A., Cihlar, J., Li, Z., 2002. Effects of spectral response function on surface reflectance and NDVI measured with moderate resolution satellite sensors. Remote Sens. Environ. 81, 1–18.

Vrieling, A., Meroni, M., Shee, A., Mude, A.G., Woodard, J., de Bie, C.A.J.M., Rembold, F., 2014. Historical extension of operational NDVI products for livestock insurance in Kenya. Int. J. Appl. Earth Obs. Geoinf. 28, 238–251. http://dx.doi.org/10.1016/j.jag.2013.12.010.

Walthall, C.L., Norman, J.M., Welles, J.M., Campbell, G., Blad, B.L., 1985. Simple equation to approximate the bidirectional reflectance from vegetative canopies and bare soil surfaces. Appl. Opt. 24, 383–387. http://dx.doi.org/10.1364/AO.24.000383.

Wang, D., Morton, D., Masek, J., Wu, A., Nagol, J., Xiong, X., Levy, R., Vermote, E., Wolfe, R., 2012. Impact of sensor degradation on the MODIS NDVI time series. Remote Sens. Environ. 119, 55–61. http://dx.doi.org/10.1016/j.rse.2011.12.001.

Willmott, C.J., 1981. On the validation of models. Phys. Geogr. 2, 184–194.

Wolters, E., Swinnen, E., Toté, C., Sterckx, S., 2016. SPOT-VGT Collection 3 Products User Manual. (VITO).

Zhang, Y., 2003. Monthly burned area and forest fire carbon emission estimates for the Russian Federation from SPOT VGT. Remote Sens. Environ. 87, 1–15. http://dx.doi.org/10.1016/S0034-4257(03)00141-X.